This is a preprint, the final version is subject to change, of the American Mineralogist (MSA)
Cite as Authors (Year) Title. American Mineralogist, in press.
DOI: https://doi.org/10.2138/am-2019-6694

Revision-1

2018-09-08

Anomalous elastic behavior of phase Egg, $AlSiO_3(OH)$, at high pressures

Mainak Mookherjee[1], Wendy R. Panero[2], Bernd Wunder[3], Sandro Jahn[4]

[1]Earth, Ocean and Atmospheric Sciences, Florida State University, Tallahassee, FL 32306

[2]School of Earth Sciences, Ohio State University, Columbus, OH 43210

[3]Deutsches GeoForschungsZentrum GFZ, Telegrafenberg, 14473 Potsdam, Germany

[4]Institut für Geologie und Mineralogie, Zülpicher Str. 49b, Universität zu Köln, 50674 Cologne, Germany

[*]Email: mmookherjee@fsu.edu

Abstract

Phase Egg ($AlSiO_3(OH)$), is an aluminosilicate hydrous mineral that is thermodynamically stable in lithological compositions represented by Al_2O_3-SiO_2-H_2O (ASH) ternary i.e., a simplified ternary for the mineralogy of subducted sediments and continental crustal rocks. High- pressure and high-temperature experiments on lithological compositions resembling hydrated sedimentary layers in subducting slabs show that phase Egg is stable up to pressures of 20-30 GPa which translates to transition zone to lower mantle depths. Thus phase Egg is a potential candidate for transporting water into the Earth's mantle transition zone. In this study, we use *first-principles* simulations based on density functional theory to explore the pressure dependence of crystal structure and how it influences energetics and elasticity. Our results indicate that phase Egg exhibits anomalous behavior of the pressure dependence of the elasticity at mantle transition zone depths (~ 15 GPa). Such anomalous behavior in the elasticity is related to changes in the

hydrogen bonding O-H…O configurations, which we delineate as a transition from a low-pressure to a high-pressure structure of phase Egg. Full elastic constant tensors indicate that phase Egg is very anisotropic resulting in a maximum anisotropy of compressional wave velocity, AV_P ~ 30 % and of shear wave velocity, AV_S ~17 % at zero pressures. Our results also indicates that the phase Egg has one of the fastest bulk sound velocities (V_P and V_S) compared to other hydrous aluminous phases in the ASH ternary, which include topaz-OH, phase Pi, and δ-AlOOH. However, the bulk sound velocity of phase Egg is slower than that of stishovite. At depths corresponding to the base of mantle transition zone, phase Egg decomposes to a mixture of δ-AlOOH and stishovite. The changes in compressional ΔV_P and shear ΔV_S velocity associated with the decomposition is ~ 0.42 % and -1.23 % respectively.

Key-words: Phase Egg, equation of state, elasticity, anisotropy, symmetric hydrogen bonding, subduction zone

Introduction

Based on estimates of planetary accretion, geochemistry, and the influx and outgassing of water, it is evident that our understanding of the size of the deep mantle reservoir of water is far from complete. Water is absolutely essential for the sustenance of planetary activities, including melting (Hirschmann, 2006) that eventually leads to large-scale geochemical differentiation. Water also helps in sustaining planetary geodynamics. In particular, water affects transport properties including the rheology (Mei and Kohlstedt, 2000), viscosity (*e.g.*, Ichikawa et al., 2015) and electrical conductivity (*e.g.*, Wang et al., 2006). Without water the mantle convection processes for a dry silicate rock will be extremely sluggish. Therefore, it is important to estimate

the size of such a water reservoir in the deep Earth. Knowing the extent of mantle hydration is also likely to enhance understanding of the role of solid Earth in influencing the sea level over long time scales (~10^9 years). However, constraining the water content of the deep Earth is not straightforward. It is important to estimate how water is transported into the deep Earth and the water-storage potential and stability of minerals and rocks at deep Earth conditions, which is an upper bound of possible water content. Estimation of actual water storage requires geophysical observations of elasticity and electrical conductivity of the deep Earth and the effect of water on those physical properties.

Most of the mantle consists of nominally anhydrous minerals (NAMs) with trace quantities of water, which are thermodynamically stable along a normal mantle geotherm i.e., do not readily decompose at these temperatures. Hydrous mineral phases are distinct from the NAM phases and contain structurally bound hydroxyl groups i.e., OH^- groups occur in well-defined crystallographic sites (Smyth, 2006). Although, water is transported into the deep Earth via subduction of hydrated lithosphere containing hydrous mineral phases (Kawamoto, 2006), a distinct limitation for hydrous phases as potential reservoir for water over geological time scale is that they are not thermodynamically stable in a normal mantle geotherm. Hence, water is likely to be partitioned to NAMs whose water retention capacity is significantly lower. For example, while hydrous phases can host several wt % of water (Kawamoto, 2006; Mookherjee et al., 2015), at depths greater than 200 km, NAMs can host 70-700 wt ppm of H_2O as hydroxyl defects (Bolfan-Casanova, 2005).. However, based on high-pressure and high-temperature experiments it is known that aluminous hydrous phases have significantly greater thermal stability than the magnesio-silicate hydrous phases and are likely to be stable in normal mantle geotherms. The aluminous hydrous phases can be represented by the Al_2O_3-SiO_2-H_2O (ASH)

ternary i.e., a simplified ternary for the mineralogy of a subducted sedimentary layer (Peacock, 1990; Ono, 1999; Schmidt et al., 1998; Schreyer et al., 1995; Wunder et al., 1993a,b; Pamato et al., 2015). Several hydrous mineral phases are stable in the ASH ternary system. These include gibbsite ($Al(OH)_3$), diaspore (AlOOH), kaolinite ($Al_2Si_2O_5(OH)_4$), topaz-OH ($Al_2SiO_4(OH)_2$), phase Pi ($Al_3Si_2O_7(OH)_3$), phase Egg ($AlSiO_3(OH)$), and dense high-pressure phases such as δ-AlOOH. In addition, recent experimental studies suggest that the dense hydrous magnesium silicate minerals phase-D ($MgSi_2O_4(OH)_2$) could have an aluminum-rich end member with stoichiometry of $Al_2SiO_4(OH)_2$ (Pamato et al., 2015). It is estimated that the net water contribution from oceanic crust is likely to be greater than from the sediments (Peacock, 1990). However, owing to the greater thermal stability of the minerals stabilized in sedimentary layer, they may be effective in transporting water into the deep Earth in warmer subduction zones (Ono, 1998). Among these hydrous phases, phase Egg has the potential to carry water to mantle transition zone depths and as a result it has been subject of numerous investigations that elucidate its high-pressure and temperature stability and compressibility. Phase Egg was first synthesized above 10 GPa (Eggleton et al., 1978) and since then the thermodynamic stability have been investigated numerous times with the high-pressure limits ranging from 20 - 30 GPa where phase Egg decomposes to δ-AlOOH and stishovite (Schmidt et al., 1998; Ono et al., 1999; Sano et a., 2004; Fukuyama et al., 2017; Abe et al., 2018). Phase Egg has also been found as inclusions in natural diamonds from Junia, Brazil indicating that crustal materials are indeed deeply subducted to the mantle transition zone and upper part of lower mantle (Wirth et al., 2007). Although phase Egg could potentially play an important role in transporting water into the deep Earth, its elasticity remains unknown. The latter is a crucial physical property that will help us to understand the mantle hydration caused by subduction of hydrated sediments or alumina

rich crustal rocks.

In this study, we use *first-principles* simulations to explore how pressure affects the crystal structure and proton environments, equation of state, full elastic constant tensor and elastic anisotropy of phase Egg at high pressures.

Methods

Phase Egg, $AlSiO_3(OH)$, is stable at pressures greater than 11 GPa and it has a monoclinic symmetry with space group $P2_1/n$ (Schmidt et al., 1998). Based on the powder X-ray diffraction refinement of the crystal structure of phase Egg all Al and Si are located in the octahedral coordination with oxygen with one unique Si and Al site each in the unit cell (Schmidt et al., 1998). There are four crystallographically distinct positions for oxygen atoms-O(1), O(2), O(3), O(4). The O(1) and O(2) oxygen atoms are bonded to two silicon (Si) and one aluminum (Al) atoms. The O(4) atom is bonded to the proton (H), two aluminum (Al) atoms and a silicon (Si) atom. The structure consists of short chain segments connecting four edge-sharing octahedral units in the *a*-axes direction with Al-Si-Si-Al ordering in the *a*-*c* plane. These 4-member edge-sharing chains are linked in the *a*-axes direction by edge link between the AlO_6 and the neighboring SiO_6 octahedral unit (**Figure 1**). These two-dimensional sheets are then linked in the (011) direction through Al-Si corner linked octahedral unit. Hydrogen bonding bridges corners of AlO_6 units, also linking the 2D structures of the edge-sharing octahedral units. Based on ^{1}H-^{29}Si NMR spectra of phase Egg, it has been suggested that there could be some disorder of Si and Al between the octahedral sites (Xue et al., 2006).

We performed *first-principles* quantum mechanical calculations based on the density functional theory (DFT) (Hohenberg and Kohn, 1964; Kohn and Sham, 1965). For the

investigation of the phase Egg, we employed a widely used approximation to the exchange-correlation functional: the generalized gradient approximation (GGA) and the highly accurate projector augmented wave method (PAW) as implemented in the Vienna ab initio simulation package (VASP) (Kresse and Hafner, 1993; Kresse and Furthmüller, 1996a, b; Kresse and Joubert, 1999). First, we performed a series of convergence tests by varying the energy cutoff and k-points. We found that an energy cut-off E_{cut}= 800 eV and a k-point mesh of $6\times9\times6$ Monkhorst-Pack grid (Monkhorst and Pack, 1976) with 100 irreducible k-points is sufficient for describing the energetics of phase-Egg (**Supplementary Figure SF1**). We also used the van der Waals corrections as implemented in VASP (Grimme, 2006). All computations were performed on the primitive unit cell of phase Egg with the starting guess from X-ray diffraction crystal structure (Schmidt et al., 1998). To test the assertion that the Al- and Si-octahedral sites may be disordered (Xue et al., 2006), we have also explored the effect of octahedral cation disorder in which we exchanged 25 % and 50% of the Al and Si octahedral sites.

The elastic tensor was derived using the finite strain approach. Starting from the optimized cell at a given pressure, we have strained the lattice parameters by 1% and then relaxed the atomic positions and computed the corresponding stress tensor. Using Hooke's law, the elastic constants were derived from the stress-strain relations, as outlined in previous studies (Chheda et al., 2014). Finally, we computed the single crystal azimuthal anisotropy for compressional velocity (AV_P) i.e., $\left(\frac{(V_P^{max}-V_P^{min})}{(V_P^{max}+V_P^{min})}\times200\right)$ and shear velocity (AV_S) i.e., $\left(\frac{(V_S^{max}-V_S^{min})}{(V_S^{max}+V_S^{min})}\times200\right)$ of phase-Egg using the formulation for maximum polarization anisotropy (Mainprice, 1990).

Results

Crystal Structure

The converged structure has a monoclinic symmetry and space group (#14) $P2_1/c$. The crystallographic space group $P2_1/n$ is an alternate setting for $P2_1/c$. In spacegroup $P2_1/n$ the translation is along a diagonal on the plane perpendicular to 2_1-screw axis whereas the translation is along the *c*-axis on the plane perpendicular to the 2_1-screw axis. We note that the disordered phase has higher enthalpy than the ordered state by 0.5 eV, or a Gibbs free energy difference between the ordered and the disordered states at 1800 K of ~0.2 eV/molecular unit (19 kJ/mol). The enthalpy and Gibbs free energy difference remains largely insensitive to pressures (**Supplementary Figure SF2**). Since the energetic cost of disordering is slightly greater than the ordered state, we have used the ordered crystal structure for the determination of the full elastic constant tensor.

At ambient conditions, the crystal structure of phase Egg has a single proton (H) with fractional coordinates of x_H=0.796, y_H= 0.553, z_H=0.422. The proton forms a hydroxyl O(4)-H bond with the O(4) atom with fractional coordinate of x_{O4}=0.760, y_{O4}= 0.215, z_{O4}=0.129. The proton also forms a hydrogen bond H….O with the O(3) atom with fractional coordinate of x_{O3}=0.880, y_{O3}= 0.201, z_{O3}=0.512 (Schmidt et al., 1998). Our results indicate that the O(4)-H….O(3) hydrogen bond is strengthened at high pressures, the O(4)-H bond is enhanced and H….O(3) length decreases. At around ~15 GPa the proton flips its position and is transferred to the O(3) atom forming an O(3)-H group and an O(4)….H bond (**Figure 2**). This is slightly different from more conventional symmetrization of hydrogen bonds at high pressures where the proton is at the center of the O….O forming a O-H-O unit. At pressures lower than the proton transfer ~15 GPa, we define the crystal structure as the phase Egg (*loP*), and at higher pressure,

we define the crystal structure as phase Egg (*hiP*), where "*loP*" and "*hiP*" refers to low- and high-pressures respectively. The energetics and properties of the phase Egg (*hiP*) extrapolated to pressures lower than 15 GPa differs significantly from that of phase Egg (*loP*). At pressures >15 GPa the structures are identical (**Figure 2**). Our pressure volume results and the evolution of lattice parameter upon compression are in good agreement with previous experiments (Vanpeteghem et al. 2003). High-pressure symmetrization of hydrogen bond has been reported in many hydrous minerals including ice phases (Goncharov et al., 1996); δ-AlOOH (Tsuchiya et al., 2002; Panero and Stixrude, 2004; Tsuchiya and Tsuchiya, 2009; Sano-Furukawa et al., 2010; Mashino et al., 2016); δ-CrOOH analog to the δ-AlOOH phase (Jahn et al., 2012); ε-FeOOH (Otte et al., 2009); phase D (Tsuchiya et al., 2005; Hushur et al., 2011); phase H (Tsuchiya and Mookherjee, 2005; Panero and Caracas, 2017) and phase Pi (Peng et al., 2017). For symmetric hydrogen bonds, often the O-H…O angle is ~180^{o} or close to a linear arrangement. However, for phase Egg we notice that the O(4)-H…O(3) angle to be around 160^{o} at pressures where proton transfer occurs (~ 15 GPa), leading to a new configuration of O(4)…H-O(3) (**Figure 2**). In a recently examined hydrous aluminosilicate phase Pi, similar observation was made, few of the O-H…O configurations remained non-linear even after compressions, however the O-H…O configuration that exhibited symmetric hydrogen bonding at high pressure became linear (Peng et al., 2017). In addition, a new monoclinic phase of AlOOH has been predicted which has non-linear and bent O-H-O linkages instead of symmetric hydrogen bonding at high pressures (Zhong et al., 2016).

Equation of state

The volume dependence of the total energy obtained using first principles simulation are adequately described by a third order Birch-Murnaghan equation of state (Birch, 1978), where total energy, E is expressed as

$$E = E_0 + \frac{9}{2} K_0 V_0 [f_V^2 + (K_0' - 4) f_V^3] \quad (1)$$

where, E_0, K_0, V_0, and K_0' represents the ground state energy, bulk modulus at zero-pressure, unit-cell volume at zero pressure, and pressure derivative of zero-pressure bulk modulus respectively. The Eulerian finite strain (f_V) and is defined as

$$f_V = \frac{1}{2}\left(\left(\frac{V_0}{V}\right)^{\frac{2}{3}} - 1\right) \quad (2)$$

We find that the phase Egg (*loP*) has lower energy than that of the phase Egg (*hiP*). The energies of the two crystal structures approach each other gradually on expansion, becoming indistinguishable at a volume ~196 Å^3 corresponding to a pressure ~ 15 GPa. The energy vs. volume relationship of phase Egg (*loP*) and phase Egg (*hiP*) suggest that at lower pressures the asymmetric arrangement of hydrogen i.e., O(4)-H….O(3) is favored, at pressures greater than 15 GPa, the proton flips its position to O(4)…H-O(3). The energy vs. volume relationship suggests a second- order phase transition (**Figure 3**). Similar second order transitions characterized by proton-order-disorder behavior and/or hydrogen bond symmetrization have been documented for condensed phases including several H_2O-ice phases (Schweizer and Stillinger, 1980; Lee et al., 1993), dense hydrous magnesium silicate minerals phase- D (Tsuchiya et al., 2005), phase-H (Tsuchiya and Mookherjee, 2015), and δ-AlOOH aluminum oxy-hydroxide (Tsuchiya et al., 2002; Panero and Stixrude, 2004; Tsuchiya and Tsuchiya, 2009). Such second order transitions are often associated with discontinuity in second order derivatives of energy, such as bulk

206 modulus (Tsuchiya et al., 2002; Sano-Furukawa et al., 2009; Hushur et al., 2011). In contrast, the
207 pressure-volume relations for phases exhibiting second order transitions related to
208 symmetrization of hydrogen bonds are often continuous with slight or no difference in the zero
209 pressure volume between the low and high-pressure phases (for e.g., phase-D: Hushur et al.,
210 2011).

211 The bulk modulus at zero-pressure (K_0^{loP}), unit-cell volume at zero pressure (V_0^{loP}) and
212 the pressure derivative of zero-pressure bulk modulus (K'^{loP}_0) for phase Egg (*loP*) i.e., at
213 pressures below the transfer of proton are, 164.4 (±1.8) GPa, 210.21 (±0.14) Å^3, and 7.14 (±0.24)
214 respectively. The bulk modulus at zero-pressure (K_0^{hiP}), unit-cell volume at zero pressure (V_0^{hiP})
215 and the pressure derivative of zero-pressure bulk modulus (K'^{hiP}_0) for phase Egg (*hiP*) at
216 pressures above the transfer of proton are, 222.8 (±0.2) GPa, 207.74 (±0.01) Å^3, and 4.44 (±0.02)
217 respectively. The zero pressure volume of the *loP* phase Egg is ~ 1.2 % larger than the hiP phase
218 Egg. In contrast, the zero pressure bulk modulus of *loP* phase Egg is ~35.5 % softer than the *hiP*
219 phase Egg. This behavior is similar to what has been observed in equation of state studies in
220 phase-D where the zero pressure volume of the hydrogen off-centered (HOC) phase is ~2.1%
221 larger than the hydrogen centered (HC) phase (Hushur et al., 2011). In contrast the zero pressure
222 bulk modulus of the HC phase is ~18% stiffer than the HOC phase (Hushur et al., 2011).

223 The experimentally determined equation of state parameters for phase Egg, i.e., (K_0^{exp}),
224 (V_0^{exp}) and (K'^{exp}_0) are, 157.0 (±4.0) GPa, 212.99 (±0.01) Å^3, and 6.5 (±0.4) respectively
225 (Vanpeteghem et al., 2000). The unit-cell volume at zero pressure for phase Egg (*loP*)
226 determined by *first-principles* simulation is 1.3 % smaller than the experimental results.
227 Whereas, the bulk modulus at zero-pressure determined by *first-principles* simulation is 4.7 %
228 greater than the experimental results. This is expected since the experiments are at 300 K and the

first principles simulations are at static conditions (0 K). The variation of the lattice parameters, i.e., *a*, *b*, *c*, β with respect to the unit-cell volume for the low pressure and the high-pressure phase Egg determined using *first-principles* simulations agree with the experimental results (**Figure 3, Supplementary Figure SF3**). The linear moduli at zero-pressure for the lattice parameter- *a*, *b*, and c^*= *c* x $sin\beta$ i.e., K_a^{loP}, K_b^{loP}, and $K_{c^*}^{loP}$ for the phase Egg (*loP*) are 975.6 (±1.2) GPa, 344.6 (±0.6) GPa, and 531.1 (±0.8) GPa respectively. The linear moduli at zero-pressure for the lattice parameter- *a*, *b*, and c^* i.e., K_a^{hiP}, K_b^{hiP}, and $K_{c^*}^{hiP}$ for the phase Egg (*hiP*) are 815.6 (±2.8) GPa, 507.9 (±0.7) GPa, and 789.6 (±1.1) GPa (**Supplementary Figure SF4**). The proton transfer stiffens with $K_b^{hiP} > K_b^{loP}$ and $K_{c^*}^{hiP} > K_{c^*}^{hiP}$ by ~ 32 %. This stiffening is likely related to the proton transfer and the significant changes of compressibility along the *b*- and c^*-lattice directions are related to the orientation of the bent and non-linear O-H…O bonds. Upon compression, of phase Egg exhibit anomalous elastic behavior at ~15 GPa, most likely related to the observed proton transfer. Our results on equation of state and evolution of lattice parameters with pressure are in good agreement with previous experimental results (Vanpeteghem et al. 2003). The experimental results showed a strong anisotropic behavior with larger compressibility along the *b*-axis compared to the *a*- and *c*- axes directions. The measured change in the slope of compressibility in *b*-direction with significant increase in stiffness above ~19 GPa, was identified as a phase transition due to a hydrogen bond symmetrization (Sikka, 2007).

Elasticity

Monoclinic phase Egg ($P2_1/c$) has 13 non-zero independent elastic constants. Upon compression almost all the individual components of the full elastic constant tensor becomes stiffer except the off-diagonal components c_{25}, c_{35}, and c_{46} (**Figure 4**). The pressure dependence

of the elasticity data can be described with the finite strain formulation (Karki et al., 2001) (**Table 1**)

$$c_{ijkl} = (1 + 2f_V)^{\frac{7}{2}}\left[c_{ijkl0} + b_1 f_V + 2b_2 f_V^2\right] - P\Delta_{ijkl} \quad (3)$$

where, f_V is the finite Eulerian strain as defined in eq (2)

$$b_1 = 3K_0\left(c'_{ijkl0} + \Delta_{ijkl}\right) - 7c_{ijkl0}, \quad (4)$$

$$b_2 = 9K_0^2 c''_{ijkl0} + 3K'_0\left(b_1 + 7c_{ijkl0}\right) - 16b_1 - 49c_{ijkl0}, \quad (5)$$

and $\Delta_{ijkl} = -\delta_{ij}\delta_{kl} - \delta_{ik}\delta_{jl} - \delta_{il}\delta_{jk}$ (6)

where c'_{ijkl0} and c''_{ijkl0} are the first and second derivatives of c_{ijkl0}, with respect to pressure at ambient conditions. Δ_{ijkl} is equal to -3 for the principal constants (c_{iiii} in full tensor and c_{ii} in Voigt notation, with i= 1, 2, 3), -1 for the off-diagonal elastic constants (c_{iijj} in full tensor and c_{ij} in Voigt notation, with i=1, 2, 3, $i \neq j$), -1 for the shear constants (c_{ijij} in full tensor notation with i =1, 2, 3, $i \neq j$ and c_{ij} in Voigt notation with i = 4, 5, 6, $i = j$), and 0 otherwise. δ_{ij} is the Kronecker delta (δ_{ij}= 1 for i=j, and δ_{ij}= 0, for i≠j).

At around ~15 GPa, i.e., pressure corresponding to mantle transition zone, many components of the full elastic constant tensor exhibit anomalous behavior. At pressure greater than 15 GPa, all components of the elastic constants become stiffer. This anomalous behavior in elasticity is very likely related to the changes in the hydrogen bonding, in particular the proton attached to O(4) atom flips to the O(3) atom. We analyzed the elasticity phase-Egg (*loP*) for pressures below the proton transfer (~ 15 GPa). And we also determined the elasticity of phase Egg (*hiP*) for pressure > 15 GPa. We note that at low pressures, there is significant difference between several components of the elastic constant tensor between the phase-Egg (*loP*) and the metastable extension of elasticity of phase Egg (*hiP*) to pressures below 15 GPa. At pressures

greater than 15 GPa, elasticity of phase Egg (*loP*) and phase Egg (*hiP*) are identical (**Figure 4**). At zero-pressures conditions the principal elastic constants exhibit the relationship: $c_{11}^{loP} > c_{33}^{loP} > c_{22}^{loP}$. The same relationship holds for the zero-pressure metastable extension of high-pressure phase Egg (*hiP*), i.e., $c_{11}^{hiP} > c_{33}^{hiP} > c_{22}^{hiP}$. We also note that the $c_{11}^{hiP} \sim c_{11}^{loP}$, $c_{33}^{hiP} > c_{33}^{loP}$ by 14 % and $c_{22}^{hiP} > c_{22}^{loP}$ by 30 %. This consistent with the fact that the orientation of the hydrogen bond is mostly aligned along the *b*-axis but is tilted such that it has component along the *c*-axis of the crystal structure. The crystallographic *a*-axis direction remains largely unaffected by the proton transfer. We also note that at pressures lower than the proton transfer pressures (~15 GPa), the pressure derivatives for the principal elastic constants $c_{ii}'^{loP} > c_{ii}'^{hiP}$, by 19 %, 29 %, and 58 % for $i = 1, 2,$ and 3 respectively.

For the shear elastic components i.e., i = 4, 5, 6, $i = j$, at zero pressure conditions, the following relations holds $c_{44}^{loP} < c_{66}^{loP} < c_{55}^{loP}$. Similar relationship holds for the zero-pressure metastable extension of phase Egg (*hiP*): $c_{44}^{hiP} < c_{66}^{hiP} < c_{55}^{hiP}$. However, unlike the principal components, the shear components have different relationship between the low-pressure phase Egg (*loP*) and the metastable extension of high-pressure phase Egg (*hiP*), $c_{44}^{hiP} \sim c_{44}^{loP}$, $c_{66}^{hiP} < c_{66}^{loP}$ by 1.8 % and $c_{55}^{hiP} < c_{55}^{loP}$ by 2.4 %. We also note that at P < 15 GPa, the pressure derivatives for the shear elastic constants $c_{ij}'^{loP} > c_{ij}'^{hiP}$, by 33 %, 28 %, and 28 % for i = 4, 6, and 5, ($i = j$) respectively.

Our results show that the phase Egg exhibits significant elastic anisotropy (**Figure 5**). The P-wave azimuthal and S-wave anisotropy for phase Egg for the phase Egg (*loP*) are AV_P ~ 30% and AV_S ~17 % at 0 GPa. The anisotropy reduces at high pressure and then increases closer to the proton transition pressures ~15 GPa. At pressures greater than 15 GPa, AV_P ~ 10% and AV_S ~10 % and remains unchanged at higher pressures (**Figure 5**).

297 The isotropic bulk (K) and shear (G) moduli are determined using the relations

298 $$K_V = \left(\frac{1}{9}\right)[c_{11} + c_{22} + c_{33} + 2(c_{12} + c_{13} + c_{23})] \quad (7)$$

299 $$K_R = [s_{11} + s_{22} + s_{33} + 2(s_{12} + s_{13} + s_{23})]^{-1} \quad (8)$$

300 $$G_V = \left(\frac{1}{15}\right)[c_{11} + c_{22} + c_{33} - (c_{12} + c_{13} + c_{23}) + 3(c_{44} + c_{55} + c_{66})] \quad (9)$$

301 and $$G_R = 15[4(s_{11} + s_{22} + s_{33}) - (s_{12} + s_{13} + s_{23}) + 3(s_{44} + s_{55} + s_{66})]^{-1} \quad (10)$$

302 where s_{ijkl} represents the elastic compliance tenor and is related c_{ijkl} by the relation
303 $s_{ijkl}c_{klmn} = \delta_{im}\delta_{jn}$, subscript V and R represents Voigt and Reuss bounds.

304 The Voigt limit of the bulk (K_V^{hiP}) and shear (G_V^{hiP}) moduli at zero-pressure for phase Egg (*hiP*)
305 are 229 GPa and 159 GPa respectively. In contrast, the Voigt limit of the bulk (K_V^{loP}) and shear
306 (G_V^{loP}) moduli at zero-pressure for low- pressure phase Egg (*loP*) are 201 GPa and 151 GPa
307 respectively. Thus the Voigt limit for the phase Egg (*hiP*) is greater than phase Egg (*loP*) by 14
308 % and 6 % respectively. And the Reuss limit of the bulk (K_R^{hiP}) and shear (G_R^{hiP}) moduli for the
309 phase Egg (*hiP*) are 223 GPa and 157 GPa respectively. In contrast, the Reuss limit of the bulk
310 (K_V^{loP}) and shear (G_V^{loP}) moduli for the phase Egg (*loP*) are 165 GPa and 142 GPa respectively.
311 Thus the Reuss limit for the phase Egg (*hiP*) is greater than phase Egg (*loP*) by ~35 % and 10 %
312 respectively.

313

314 **Discussions**

315 The mineral phases in the Al_2O_3-SiO_2-H_2O (ASH) ternary show correlation between velocity and
316 density. Stishovite and corundum are the densest phase and have fastest bulk sound velocity.
317 Among the hydrous phases, phase Egg (~7.5 wt % H_2O) and δ-AlOOH (~15 wt % H_2O) are the
318 densest and also have fast sound wave velocity (**Table 2, Figure 6**). Along the SiO_2-AlOOH
319 join, we note that the zero pressure density follows the trend: $\rho_0^{pi} < \rho_0^{top-o} < \rho_0^{egg-loP} <$

320 $\rho_0^{\delta-loP} < \rho_0^{st}$. Also, along the SiO_2-AlOOH join, the compressional velocity (V_P) extrapolated to
321 zero pressure, the following trend is observed $V_P^{pi} < V_P^{top-o} < V_P^{\delta-loP} < V_P^{egg-loP} < V_P^{st}$.
322 Similar trends for shear (V_S) velocity extrapolated to zero pressure i.e., $V_S^{pi} < V_S^{top-o} <$
323 $V_S^{\delta-loP} < V_S^{egg-loP} < V_S^{st}$ is also observed (**Table 2**, **Figure 6**). The observed trend in the
324 density, and shear wave velocity could be explained in terms of the crystal structures. For
325 instance, the crystal structure of phase-Pi, that is stable at relatively low pressures between 2 and
326 7 GPa (Wunder et al., 1993a,b), consists of layers of distorted eight-membered rings formed by
327 AlO_6 units alternating with layers consisting of SiO_4 tetrahedral units (Peng et al., 2017). Crystal
328 structure of topaz-OH, that is stable up to 12 GPa (Ono, 1998), also consists of edge sharing
329 AlO_6 octahedral units forming crankshaft chains and SiO_4 tetrahedral units sharing corners. In
330 contrast, phase Egg is formed at higher pressures and has both aluminum and silicon in
331 octahedral coordination. The zero pressure density of phase Egg (*loP*) is slightly greater than the
332 expected density based on an ideal solid solution of SiO_2 and δ-AlOOH (*loP*). The δ-AlOOH
333 (*loP*) refers to the hydrogen in off-center position (HOC), i.e., asymmetric hydrogen bond at
334 low- pressure condition (Tsuchiya and Tsuchiya, 2009). The compressional velocity (V_P) and
335 shear velocity (V_S) extrapolated to zero pressure for phase Egg (*loP*) is lower than the expected
336 V_P and V_S based on an ideal solid solution of SiO_2 and δ-AlOOH (*loP*) by 6.3 and 6.5 %
337 respectively (**Figure 6**).
338
339 **Implications**
340 In a simplified ASH system, at the base of the mantle transition zone and along a warm
341 subduction zone geotherm phase Egg decomposes to a mixture of aluminum oxyhydroxide (δ-
342 AlOOH) and stishovite (SiO_2) via the reaction-

$AlSiO_3(OH)$ = δ-AlOOH + SiO_2 (11)

(phase Egg (*hiP*)) (aluminum oxyhydroxide) (stishovite)

This is likely to be associated with ΔV_P and ΔV_S of 0.42 % and -1.23 % respectively. Among all the hydrous phases in the ASH ternary system, Phase Egg has one of the fastest compressional (V_P) and shear (V_S) velocity (**Figure 7**). The velocity of phase Egg is slower than stishovite but remains faster than δ-AlOOH phase at all the pressures within phase-Egg's thermodynamic stability field. The δ-AlOOH phase with symmetric hydrogen bonding has sound wave velocities faster than phase-Egg, however that is likely to occur at pressures corresponding to the lower mantle. In our analysis, we have used compressional (V_P) and shear (V_S) velocity of δ-AlOOH (Tsuchiya and Tsuchita, 2009) and stishovite (Karki et al., 1997). The static sound wave velocity results from the *first-principles* studies, are in very good agreement with experimental studies including static Brillouin scattering experiments on stishovite (Jiang et al., 2009) and δ-AlOOH (Mashino et al., 2016).

The decomposition of phase Egg at the base of the transition zone along a warmer subduction zone geotherm is ~ 1000 ^{o}C (Wirth et al., 2007). It is likely that the temperature will affect the bulk sound velocity of all the hydrous phases including phase Egg. The effect of temperature on the elasticity and seismic velocities of the hydrous phases in ASH ternary remains mostly unknown, except for stishovite (Yang et al., 2014). The effect of temperatures on compressional (V_P) and shear (V_S) velocity for natural topaz containing both hydrogen and fluorine have been recently constrained and are of the order of $\frac{dV_P}{dT}$ ~-3.10 x 10^{-4} and $\frac{dV_S}{dT}$ ~-2.30 x 10^{-4} (Tennakoon et al., 2018). The effect of temperature on the elasticity of phase Egg (*loP*) and its high-pressure polymorph, phase Egg (*hiP*) across the proton transfer needs to be constrained in future work. Presence of minor amount of fluorine $(F^-)^-$ have been speculated in a

mantle minerals in transition zone (Grützner et al., 2018). Substitution of OH-1 by fluorine (F^-) occurs in natural minerals including topaz and recent study shows that such substitution does indeed influence the bulk sound velocity (Tennakoon et al., 2018).

The sound wave velocity of phase Egg is significantly faster than the major mantle phases such as wadsleyite (Zha et al., 1997), ringwoodite (Li, 2003), pyrope (Sinogeikin and Bass, 2000), and majoritic garnet (Irifune et al., 2008) stable in the transition zone. Few wt % of water tends to reduce the seismic velocity of wadsleyite (Mao et al., 2008) and ringwoodite (Panero, 2010; Wang et al., 2006). Whereas, phase Egg could host almost 7.5 wt% of water and yet have significantly faster velocity compared to hydrous wadsleyite (Mao et al., 2008) and ringwoodite (Wang et al., 2006). Although the presence of phase Egg is likely to be limited mostly in the subducted sediments, it could store several wt % of water and be stable in a normal mantle geotherm and may not be readily detectable owing to its faster velocity compared to the ambient mantle. Certainly, more research is warranted to have better constraints on the effect of temperature, anisotropy, petrographic fabric or lattice preferred orientations on the seismic velocity of phase Egg and other mineral phases in subducted sediments.

Acknowledgements

MM acknowledges the funding support from US National Science Foundation grant (EAR-1634422; EAR-1753125), Ralph E Powe Junior Faculty Enhancement award, Oak Ridge Associated University (ORAU), and computing resources from the Extreme Science and Engineering Discovery Environment (XSEDE), which is supported by National Science Foundation grant number OCI-1053575. WRP acknowledges the funding support from the

National Science Foundation CAREER grant (EAR-60023026), and computational time from the Ohio Supercomputer Center (PAS-0238-1).

391 **References**

392 Abe, R., Shibazaki, Y., Ozawa, S., Ohira, I., Tobe, H., and Suzuki, A. (2018) In-situ X-ray
393 diffraction studies of hydrous aluminosilicate at high pressure and temperature. Journal of
394 Mineralogical and Petrological Sciences, 113, 106-111.

395 Birch, F., (1978) Finite strain isotherm and velocities for single crystal and polycrystalline NaCl
396 at high-pressures and 300 K. Journal of Geophysical Research, 83, 1257-1268.

397 Bolfan-Casanova, N. (2005) Water in the Earth's mantle. Mineralogical Magazine, 69, 229-257.

398 Chheda, T. Mookherjee, M., Mainprice, D., dos Santos, A. M., Molaison, J. J., Chantel, J.,
399 Manthilake, G., and Bassett, W. A., (2014) Structure and elasticity of phlogopite under
400 compression: Geophysical implications. Physics of the Earth and Planetary Interior,
401 233,1-12.

402 Eggleton, R. A. Boland, J. N., and Ringwood, A. E., (1978) High pressure synthesis of a new
403 aluminum silicate: $Al_5Si_5O_{17}(OH)$. Geochemichial Journal, 12, 191-194. Fukuyama, K.,
404 Ohtani, E., Shibazaki, Y., Kagi, H., and Suzuki, A. (2017) Stability field of phase Egg,
405 $AlSiO_3OH$ at high pressure and high temperature: possible water reservoir in mantle
406 transition zone. Journal of Mineralogical and Petrological Sciences, 112, 31-35.

407 Goncharov, A.F., Struzhkin, V. V., Somayazulu, M. S., Hemley, R. J., and Mao, H. K. (1996)
408 Compression of ice to 210 gigapascals: Infrarerd evidence for a symmetric hydrogen-
409 bonded phase. Science, 273, 218-220.

410 Grimme, S. (2006) Semiempirical gga-type density functional constructed with a long-range
411 dispersion correction. Journal of Computational Chemistry, 27, 1787.

412 Grützner, T., Klemme, Rohrbach, A., Grevasoni, F., and Berndt, J. (2018) The effect of fluorine
413 on the stability of wadsleyite: Implication for the nature and depths of the transition zone
414 in the Earth's mantle. Earth and Planetary SciencesLetters, 482, 236-244.
415 Hirschmann, M.(2006) Water, melting, and the deep Earth H_2O cycle. Annual Reviews of Earth
416 and Planetary Sciences, 34, 629-653.
417 Hohenberg, P., Kohn, W. (1964) Inhomogeneous electron gas. Physical Review B, 136, B864-
418 871.
419 Hushur, A., Manghnani, M. H., Smyth, J. R., Williams, Q., Hellebrand, E., Lonappan, D., Ye,
420 Y., Dera, P., and Frost, D. J. (2011) Hydrogen bond symmetrization and equation of state
421 of phase D. Journal of Geophysical Research, 116, B06203.
422 Ichikawa, H., Kawai, K., Yamamoto, S., and Kameyama, M. (2015) Effect of water on
423 subduction of continental materials to the deep Earth, in "The Earth's Heterogenous
424 Mantle" edited by Khan, A. and Deschamps, F. 275-299.
425 Irifune, T., Higo, Y., Inoue, T., Kono, Y., Ohfuji, H., and Funakoshi, K. (2008) Sound velocities
426 of majorite garnet and composition of the mantle transition region. Nature, 451, 814-817.
427 Jahn, S., Wunder, B., Koch-Müller, M., Tarrieu, L., Pöhle, M., Watenphul, A., and Taran, M.N.
428 (2012) Pressure-induced hydrogen bond symmetrisation in guyanaite, β-CrOOH:
429 evidence from spectroscopy and ab initio simulations. European Journal of Mineralogy,
430 24, 839-850.
431 Jiang, F., Majzlan, J., Speziale, S., He, D., and Duffy, T.S.(2008) Single-crystal elasticity of
432 diaspore, AlOOH, to 12 GPa by Brillouin scattering. Physics of the Earth and Planetary
433 Interior, 170, 221-228.

434 Jiang, F.,Gwanmesia, G. D.m Dyuzheva, T. I., and Duffy, T. S. (2009) Elasticity of stishovite
435 and acoustic mode softening under high pressure by Brillouin scattering. Physics of the
436 Earth and Planetary Interior, 172, 235-240.
437 Karki, B.B., Stixrude, L., Crain, J. (1997) Ab initio elasticity of three high-pressure polymorphs
438 of silica. Geophysical Research Letters, 24, 3269–3272.
439 Karki, B.B., Stixrude, L., Wentzcovitch, R.M. (2001) High-pressure elastic properties of major
440 materials of Earth's mantle from first principles. Reviews of Geophysics, 39, 507–534.
441 Katahara, K.W.(1996) Clay mineral elastic properties. SEG Annual Meeting Expanded abstracts,
442 1691-1694 http://dx.doi.org/10.1190/1.1826454.
443 Kawamoto, T. (2006) Hydrous phases and water transport in the subducting slab. Reviews Of
444 Mineralogy and Geochemistry, 62, 85-116.
445 Kohn, W., and Sham, L. J.(1965) Self-consistent equations including exchange and correlation
446 effects. Physical Review, 140, A1133-A1138.
447 Kresse, G., and Furthmüller, J. (1996a) Efficiency of ab-initio total energy calculations for
448 metals and semiconductors. Computational Material Sciences, 6, 15-50.
449 Kresse, G., and Furthmüller, J. (1996b) Efficient iterative schemes for ab initio total-energy
450 calculations using plane-wave basis set. Physical Review B 54, 11169-11186.
451 Kresse, G., and Hafner, J.(1993) Ab initio Molecular Dynamics for Liquid-Metals. Physical
452 Review B 47, 558-561.
453 Kresse, G., Joubert, D. (1999) From ultrasoft pseudopotentials to the projector augmented-wave
454 method. Physical Review B, 59, 1758-1775.
455 Lee, C., Vanderbilt, D., Laasonen, K., Car, R., and Parrinello, M. (1993) Ab initio studies on the
456 structural and dynamical properties of ice. Physical Review B, 47, 4863-4872.

Li, B. (2003) Compressional and shear wave velocities of ringwoodite γ-Mg_2SiO_4 to 12 GPa. Americal Mineralogist, 88, 1312-1317.

Mainprice, D. (1990) An efficient FORTRAN program to calculate seismic anisotropy from the lattice preferred orientation of minerals. Computational Gesoscience, 16, 385-393.

Mao, Z., Jacobsen, S. D., Jiang, F., Smyth, J. R., Holl, C. M., and Duffy, T. S. (2008) Elasticity of hydrous wadsleyite to 12 GPa: Implications for Earth's transition zone. Geophysical Research Letters, 35, L21305, doi:10.1029/2008GL035618.

Mashino, I., Murakami, M., and Ohtani, E. (2016) Sound velocities of δ-AlOOH up to core-mantle boundary pressures with implications for the seismic anomalies in the deep mantle. Journal of Geophysical Research- Solid Earth, 121, 595–609, doi:10.1002/2015JB012477

Mei, S., and Kohlstedt, D. L. (2000) Influence of water on plastic deformation of olivine aggregates 1. Diffusion creep regime. Journal of Geophysical Research, 105, 21,457-21,469.

Monkhorst, H. J., and Pack, J. D. (1976) Special points for Brillouin-zone integrations. Physical Review B, 13, 5188-5192.

Mookherjee, M., Speziale, S., Marqardt, H., Jahn, S., Wunder, B., Koch-Müller, M., Liermann, H.-P. (2015) Equation of state and elasticity of the 3.65 Å phase: implications for the X-discontinuity. American Mineralogist, 100, 2199-2208.

Mookherjee, M., Tsuchiya, J., and Hariharan, A. (2016) Crystal structure, equation of state, and elasticity of hydrous aluminosilicate phase, topaz-OH ($Al_2SiO_4(OH)_2$) at high pressures. Physics of the Earth and Planetary Interior, 251, 24-35.

Nye, J. F. (1985) Physical properties of crystals. Oxford University Press, Clarendon.

Ono, S. (1998) Stability limits of hydrous minerals in sediment and mid-ocean ridge basalt compositions: Implications for water transport in subduction zones. Journal of Geophysical Research, 103, 18253-18267.

Ono, S. (1999) High temperature stability of phase egg, $AlSiO_3(OH)$. Contribution to Mineralogy and Petrology, 137, 83-89.

Otte, K., Pentcheva, R., Schmal, W.W., and Rustad, J. R. (2009) Pressure-induced structural and electronic transitions in FeOOH from first principles. Physical Review B. 80, 205116.

Pamato, M.G., Myhill, R., Boffa Ballaran, T., Frost, D.J., Heidelbach, F. and Miyajima, N. (2015) Lower-mantle water reservoir implied by the extreme stability of hydrous aluminosilicate. Nature Geosciences, 8, 75-79.

Panero, W. R. and Stixrude, L. (2004) Hydrogen incorporation in stishovite at high pressure and symmetric hydrogen bonding in δ-AlOOH. Earth and Planetary Science Letters, 221, 421-431.

Panero, W. R. (2010) First principles determination of the structure and elasticity of hydrous ringwoodite. Journal of Geophysical Research, 115, B03203, doi:10.1029/2008JB006282.

Panero, W. R., and Caracas, R. (2017) Stability of phase H in the $MgSiO_4H_2$–AlOOH–SiO_2 system. Earth and Planetary Science Letters., 463, 171-177.

Peacock, S. M. (1990) Fluid processes in subduction zones. Science, 248, 329-337.

Peng, Y., Mookherjee, M., Hermann, A., Bajgain, S., Liu, S., and Wunder, B. (2017) Elasticity of phase-Pi ($Al_3Si_2O_7(OH)_3$)- A hydrous aluminosilicate phase. Physics of the Earth and Planetary Interior, 269, 91-97, https://doi.org/10.1016/j.pepi.2017.05.016.

Perdew, J. P., Burke, K., and Erzerhof, M. (1996) Generalized gradient approximation made simple. Physical Review Letters, 77, 3865-3868.

Sano, A., Ohtani, E., Kubo, T. and Funakoshi, K.-i. (2004) In situ X-ray observation of decomposition of hydrous aluminum silicate $AlSiO_3OH$ and aluminum oxide hydroxide δ-AlOOH at high pressure and temperature. Journalof Physics and Chemistry of Solids, 65, 1547-1554.

Sano-Furukawa, A., Kagi, H., Nagai, T., Nakano, S., Ushijima, D., Iizuka, R., Ohtani, E., and Yagi, T. (2009) Change in compressibility of δ-AlOOH and δ-AlOOD at high pressure: A study of isotope effect and hydrogen-bond symmetrization. American Mineralogist, 94, 1255-1261.

Schmidt, M. W., Finger, L. W., Angel, R. J., and Robert, E. (1998) Synthesis, crystal structure and phase relations of $AlSi_3OH$, a high pressure hydrous phase. American Mineralogist, 83, 881-888.

Schreyer, W. (1995) Ultradeep metamorphic rocks: The retrospective viewpoint. Journal of Geophysical Research, 100, 8353-8366.

Schweizer, K. S., and Stillinger, F. H. (1980) High pressure phase transitions and hydrogen-bond symmetry in ice polymorphs. Journal of Chemical Physics, 80, 1230-1240.

Sikka, S.K. (2007) On some bond correlations at high pressures. High Pressure Research, 27, 313-319.

Sinogeikin, S.V., and Bass, J.D. (2000) Single-crystal elasticity of pyrope and MgO to 20 GPa by Brillouin scattering in the diamond cell. Physics of the Earth and Planetary Interior, 120, 43-62.

524 Smyth, J.(2006) Hydrogen in high-pressure silicate and oxide mineral structures. Reviews of
525 Mineralogy and Geochemistry, 62, 85-116.
526 Tennakoon, S., Peng, Y., Mookherjee, M., Speiale, S., Manthilake, G., Besara, T., Andreu, L.,
527 and Rivera, F. (2018) Single crystal elasticity of natural topaz at high-temperatures.
528 Scientific Reports, 8, 1372, doi:10.1038/s41598-017-17856-3.
529 Tsuchiya, J., Tsuchiya, T., Tsuneyuki, S., and Yamanaka, T. (2002) First principles calculation
530 of high-pressure hydrous phase, δ-AlOOH. Geophysical Research Letters, 29, 1909.
531 Tsuchiya, J., Tsuchiya, T., and Tsuneyuki, S. (2005) First-principles study of hydrogen bond
532 symmetrization of phase D under high pressure. American Mineralogist, 90, 44-49.
533 Tsuchiya, J., and Tsuchiya, T. (2009) Elastic properties of δ-AlOOH under pressure: First
534 principles investigation. Physics of the Earth and Planetary Interior, 174, 122-127.
535 Tsuchiya, J., and Mookherjee, M. (2015) Crystal structure, equation of state, and elasticity of
536 phase H ($MgSiO_4H_2$) at Earth's lower mantle pressures. Scientific Reports, 5, 15534,
537 https://doi.org/10.1038/srep15534.
538 Tulk, C.A., Gagnon, R.E., Kiefte, H., and Clouter, M.J. (1994) Elastic constants of ice III by
539 Brillouin spectroscopy. Journal of Chemical Physics, 101, 2350.
540 Vanpeteghem, C. B. Ohtani, E. Kondo, T. Takemura, K. and Kikegawa, T. (2003)
541 Compressibility of phase Egg $AlSiO_3(OH)$: Equation of state and role of water at high
542 pressure. American Mineralogist, 88, 1408-1411.
543 Vaughan, M.T., and Weidner, D.J. (1978) The relationship of elasticity and crystal structure in
544 andalusite and sillimanite. Physics and Chemistry of Mineralals, 3, 133–144.
545 Wang, D. J., Mookherjee, M., Xu, Y., and Karato, S. (2006) The effect of water on the electrical
546 conductivity of olivine. Nature, 443, 977-980.

Wang, J., Sinogeikin, S. V., Inoue, T., and Bass, J. D. (2006) Elastic properties of hydrous ringwoodite at high-pressure conditions. Geophysical Research Letters, 33, L14308, doi:10.1029/2006GL026441.

Weidner, D.J., and Carleton, H.R. (1977) Elasticity of coesite. Journal of Geophysical Research, 82, 1334-1346.

Winkler, B., Hytha, M., Warren, M.C., Milman, V., Gale, J.D., and Schreuer, J. (2001) Calculation of the elastic constants of the Al_2SiO_5 polymorphs andalusite, silimanite and kyanite. Zeitschrift für Kristallographie, 216, 67–70.

Wirth, R., Vollmer, C., Brenker, F., Matsyuk, S., and Kaminsky, F. (2007) Inclusion of nanocrystalline hydrous aluminum silicate "Phase Egg" in superdeep diamonds from Junia (Mato Grosso State, Brazil). Earth and Planetary Science Letters, 259, 384-399.

Wunder, B., Medenbach, O., Krause, W., and Schreyer, W. (1993a) Synthesis, properties and stability of $Al_3Si_2O_7(OH)_3$ (phase Pi), a hydrous high-pressure phase in the system Al_2O_3-SiO_2-H_2O (ASH). European Journal of Mineralogy, 5, 637-649.

Wunder, B., Rubie, D. C., Ross-II, C. R., Medenbach, O., Seifert, F., and Schreyer, W. (1993b) Synthesis, stability, and properties of $Al_2SiO_4(OH)_2$: A fully hydrated analogue of topaz. American Mineralogist, 78, 285-297.

Xue, X., Kanzaki, M., Fukui, H., Ito, E., & Hashimoto, T. (2006) Cation order and hydrogen bonding of high-pressure phases in the Al_2O_3-SiO_2-H_2O system: An NMR and Raman study. American Mineralogist, 91, 850-861.

Yang, R., and Wu, Z. (2014) Elastic properties of stishovite and the $CaCl_2$-type silica at the mantle temperature and pressure: An ab inito investigation. Earth and Planetary Science Letters, 404, 14-21.

570 Zhong, X., Hermann, A., Wang, Y., and Ma, Y. (2016) Monoclinic high-pressure polymorph of
571 AlOOH predicted from first principles. Physical Review B, 94, 224110.
572

573 **Figure Captions**

574 **Figure 1.** Crystal structure of phase Egg: (***a***) projection down the *b*-axis, and (***b***) projection down
575 the *a*-axis. The octahedral units i.e., AlO_6 and SiO_6 are represented by grey and light blue
576 spheres respectively. The hydrogen atoms and the oxygen atoms are shown as silver and
577 red spheres respectively.

578 **Figure 2.** (***a***) Plot of hydroxyl bond length: $d_{O(4)\text{-}H}$, hydrogen bond length: $d_{O(4)\text{-}H\text{---}O(3)}$, and
579 separation of the oxygen atoms, i.e., O(4)---O(3) vs. unit-cell volume/pressure. (***b***)
580 Hydrogen-hydrogen repulsion denoted by H---H separation distances. (***c***) The hydrogen
581 bond angle, O(4)-H---O(3). The blue and red symbols represent the low-pressure (*loP*)
582 and high-pressure (*hiP*) phase Egg.

583 **Figure 3.** (***a***) Plot of total energy, (b) pressure, (c) lattice parameters, *a* (d) lattice parameter, *b*
584 (e) lattice parameter, *c* and (f) lattice parameter, β, for low-pressure (*loP*) (blue symbols)
585 and high-pressure (*hiP*) (red symbols) phase Egg vs. unit cell volume. The grey filled
586 symbols are from X-ray diffraction results (Vanepetghem *et al*., 2000). Unit-cell volume
587 of (*loP*) (blue symbols) and high-pressure (*hiP*) (red symbols) phase Egg is also plotted
588 as a function of pressure and compared with experimental data (grey filled symbols)
589 (**Supplementary Figure SF3**). The volume/pressure dependence of the lattice parameters
590 is characteristics of a second order transition and has been documented in several hydrous
591 phases (Tsuchiya et al., 2002; 2005; Tsuchiya and Mookherjee, 2015).

592 **Figure 4.** Full elastic constant tensor (C_{ij}) components, for phase Egg as a function of pressure
593 (**Table 1**). There are 12 sub plots and an inset, representing the 13 independent elastic
594 constants for the monoclinic symmetry. The low-pressure (*loP*) and high-pressure (*hiP*)
595 phase Egg is represented by blue and red symbols respectively.

Figure 5. (**a**) Plot of elastic anisotropy AV_P and AV_S for phase Egg as a function of pressure. The low-pressure (*loP*) and high-pressure (*hiP*) phase Egg is represented by blue and red symbols respectively. The stereographic projection down the X_3 axes for AV_P, AV_S and V_S polarization planes at (***b***) ~0 GPa and (***c***) ~23 GPa.

Figure 6. (***a***) A ternary plot with Al_2O_3-SiO_2-H_2O as the end member components, relevant for the mineral phases stable in subducted sediments. Also shown is the blue shaded region along the line joining the SiO_2 and AlOOH with a series of hydrous phases, δ-AlOOH, topaz-OH, phase Egg, phase-pi and stishovite. Plot of (***b***) V_P, (***c***) V_S as a function of density for the mineral phases in the ASH ternary (**Table 2**). The vertical grey-brown shaded line demonstrates that the density of low-pressure (*loP*) and high-pressure (*hiP*) phase Egg are very similar but the velocities are distinct. This is related to the fact that second-order transition associated with the proton transfer affects the second derivative of energy, i.e., elastic constants but the volume and density remains mostly unaffected by the proton transfer. The blue and red dashed line represents linear regression fits for the compressional wave, V_P is given by $[2.77\ (\pm 0.49)\times\rho + 0.07\ (\pm 1.64)]$ and for the shear wave, V_S is given by $[1.74\ (\pm 0.27)\times\rho - 0.23\ (\pm 0.91)]$. The light blue and red lines represents 95 % confidence level for the primary and shear velocity- density regressions. Plot of zero pressure (***d***) density (***e***) V_P, and V_S for hydrous mineral phase along the SiO_2 and AlOOH join.

Figure 7. (***a***) Plot of K_H and G_H i.e., Hill averaged (average of Voigt and Reuss limits) for low-pressure (*loP*) and high-pressure (*hiP*) phase Egg represented by blue and red symbols respectively. Also shown is an experimentally determined bulk modulus in grey symbol (Vanepetghem *et al.*, 2000). (***b***) Plot of pressure dependence of V_P and V_S for low-

pressure (*loP*) and high-pressure (*hiP*) phase Egg and other mineral phases including, stishovite (Karki et al., 1997) topaz-OH (Mookherjee et al., 2016), phase Pi (Peng et al., 2017), and δ-AlOOH (Tsuchiya and Tsuchiya, 2009) that are likely stable in subducted sediments. (***c***) A pressure-temperature-depth phase diagram illustrating the stability of phase Egg. The figure is modified from previous study (Wirth et al., 2007). Also shown are the green shaded area representing the mantle transition zone. The blue shaded band at ~ 15 GPa indicates the predicted pressure for the proton transfer, i.e., boundary between phase Egg (*loP*) and phase Egg (*loP*) associated with the elastic anomaly as observed in our study. The dashed circle at the intersection of warm subduction geotherm with the high-pressure stability of phase Egg (*hiP*), where phase Egg will decompose to d-AlOOH and stishovite is likely to be associated with ΔV_P and ΔV_S of 0.42 % and -1.23 % respectively.

This is a preprint, the final version is subject to change, of the American Mineralogist (MSA)
Cite as Authors (Year) Title. American Mineralogist, in press.
DOI: https://doi.org/10.2138/am-2019-6694

Table 1. Full elastic constant tensor for low-pressure (*loP*) and high-pressure (*hiP*) phase Egg. The finite strain fits are also reported.

V	P	c_{11}^{loP}	c_{22}^{loP}	c_{33}^{loP}	c_{12}^{loP}	c_{13}^{loP}	c_{15}^{loP}	c_{23}^{loP}	c_{25}^{loP}	c_{35}^{loP}	c_{44}^{loP}	c_{55}^{loP}	c_{66}^{loP}	c_{46}^{loP}
220	-6.4	449.5	198.7	271.9	91.9	134.4	6.2	14.2	26.3	34.4	106.1	148.0	136.0	27.5
215	-3.4	473.9	243.1	345.0	92.2	135.5	6.6	56.9	18.5	25.2	130.3	161.6	147.8	22.7
210	0.2	504.7	280.4	401.0	98.6	141.6	7.5	87.9	13.5	19.8	150.3	174.0	159.7	18.6
205	4.5	538.9	314.3	448.8	109.3	152.1	9.1	113.0	10.1	16.7	168.1	186.2	171.7	15.6
200	9.8	575.4	342.7	492.7	121.9	165.4	8.8	133.6	7.3	14.9	185.5	197.3	184.3	13.1
198	12.2	590.4	334.8	508.7	125.7	171.3	9.1	135.6	7.4	14.6	192.7	201.7	189.7	12.5
196	14.7	605.0	361.7	499.1	138.1	183.7	9.8	125.9	12.7	19.2	200.7	205.4	195.6	12.3
195	16.1	608.7	467.8	555.3	143.5	188.6	4.4	192.0	-7.3	7.7	191.7	202.4	179.8	-9.7
190	23.7	653.1	519.8	600.2	169.5	212.4	5.7	221.7	-6.6	9.3	208.0	215.7	192.0	-7.5
185	32.8	701.1	573.8	648.1	198.7	238.6	7.2	252.3	-5.6	10.8	225.7	229.6	206.0	-4.6
180	43.7	752.0	627.4	699.5	228.6	267.6	8.3	284.6	-5.6	12.0	243.7	243.2	219.6	-2.9
						finite strain fit								
	c_0^{loP}	503.4	278.9	398.5	98.1	141.3	7.5	86.5	13.7	20.1	149.5	173.5	159.2	18.8
	c'^{hiP}_0	8.02	9.60	14.78	1.69	1.76	3.17	8.15	1.68	1.59	7.27	5.22	5.11	2.01
	c''^{hiP}_0	-0.141	-0.775	-1.298	0.188	0.178	-0.008	-0.839	0.168	0.222	-0.400	-0.201	-0.137	0.102
V	P	c_{11}^{hiP}	c_{22}^{hiP}	c_{33}^{hiP}	c_{12}^{hiP}	c_{13}^{hiP}	c_{15}^{hiP}	c_{23}^{hiP}	c_{25}^{hiP}	c_{35}^{hiP}	c_{44}^{hiP}	c_{55}^{hiP}	c_{66}^{hiP}	c_{46}^{hiP}
220	-11.3	431.9	281.6	380.8	65.2	110.3	2.4	81.1	-1.8	7.1	115.2	143.3	136.5	-11.6
210	-2.4	494.7	347.7	443.7	90.2	134.6	3.5	118.7	-6.2	6.8	144.8	165.5	153.1	-11.5
200	9.2	566.8	423.6	516.8	123.7	167.5	4.6	163.8	-8.9	8.2	175.0	189.2	171.1	-11.1
190	24.3	650.9	519.7	603.8	170.9	211.6	6.2	220.4	-9.1	11.3	206.9	215.0	193.0	-8.5
180	44.0	748.9	627.3	704.2	229.8	266.7	8.2	283.3	-8.3	14.5	243.2	242.3	220.1	-4.5
						finite strain fit								
	c_0^{hiP}	509.8	362.8	456.0	98.9	141.9	3.7	127.8	-6.6	7.6	150.4	169.3	156.3	-11.5
	c'^{hiP}_0	6.48	6.82	6.16	2.97	2.80	3.10	3.88	2.69	3.06	4.85	3.78	3.66	3.04
	c''^{hiP}_0	-0.068	-0.050	-0.038	-0.002	-0.001	-0.0001	-0.021	0.015	0.005	-0.044	-0.010	-0.015	0.007

This is a preprint, the final version is subject to change, of the American Mineralogist (MSA)
Cite as Authors (Year) Title. American Mineralogist, in press.
DOI: https://doi.org/10.2138/am-2019-6694

Table 2. Density, compressional (V_P), and shear (V_S) wave velocity of mineral phases in Al_2O_3-SiO_2-H_2O ternary.

Mineral	Abbreviation	Stoichiometry	ρ (g/cm^3)	V_P (km/s)	V_S (km/s)	H_2O (wt %)	Reference
Corundum	cor	Al_2O_3	3.95	10.94	6.41	0.00	Ohno et al. (1986)
Quartz	qz	SiO_2	2.64	6.09	4.12	0.00	Ohno et al. (2006)
Coesite	cs	SiO_2	2.93	8.17	4.58	0.00	Weidner and Carleton (1977)
Stishovite	st	SiO_2	4.30	11.91	7.28	0.00	Jiang et al. (2009)
Ice	ice-iii	H_2O	1.16	3.66	2.01	100.00	Tulk et al. (1994)
Andalusite	and	Al_2SiO_5	3.15	9.76	5.65	0.00	Vaughan and Weidner (1978)
Sillimanite	sil	Al_2SiO_5	3.24	9.65	5.42	0.00	Vaughan and Weidner (1978)
Kyanite	ky	Al_2SiO_5	3.76	9.68	5.87	0.00	Winkler et al. (2001)
Diaspore	dia	AlOOH	3.38	9.42	5.83	15.00	Jiang et al. (2008)
δ-AlOOH	δ-loP	AlOOH	3.39	9.82	6.19	15.00	Tsuchiya and Tsuchiya (2009)
δ-AlOOH	δ-hiP	AlOOH	3.47	10.87	6.60	15.00	Tsuchiya and Tsuchiya (2009)
Kaolinite	kl	$Al_2Si_2O_5(OH)_4$	2.52	6.23	3.55	18.19	Katahara (1996)
Topaz-OH	top-m	$Al_2SiO_4(OH)_2$	3.43	9.75	5.81	10.00	Mookherjee et al. (2016)
Topaz-OH	top-o	$Al_2SiO_4(OH)_2$	3.39	9.51	5.51	10.00	Mookherjee et al. (2016)
phase-pi	pi	$Al_3Si_2O_7(OH)_3$	3.21	8.86	5.28	9.00	Peng et al. (2017)
phase-Egg	egg-loP	$AlSiO_3(OH)$	3.79	9.99	6.22	7.50	*this study*
Phase-Egg	egg-hiP	$AlSiO_3(OH)$	3.84	10.68	6.42	7.50	*this study*

DOI: https://doi.org/10.2138/am-2019-6694

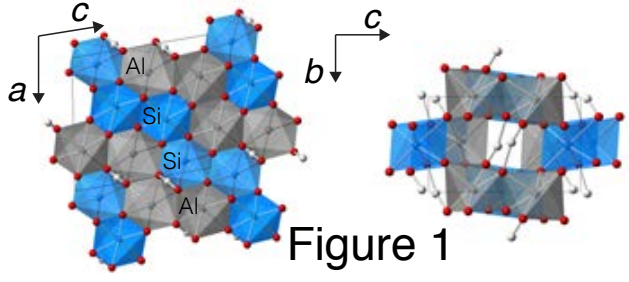

Figure 1

This is a preprint, the final version is subject to change, of the American Mineralogist (MSA)
Cite as Authors (Year) Title. American Mineralogist, in press.
DOI: https://doi.org/10.2138/am-2019-6694

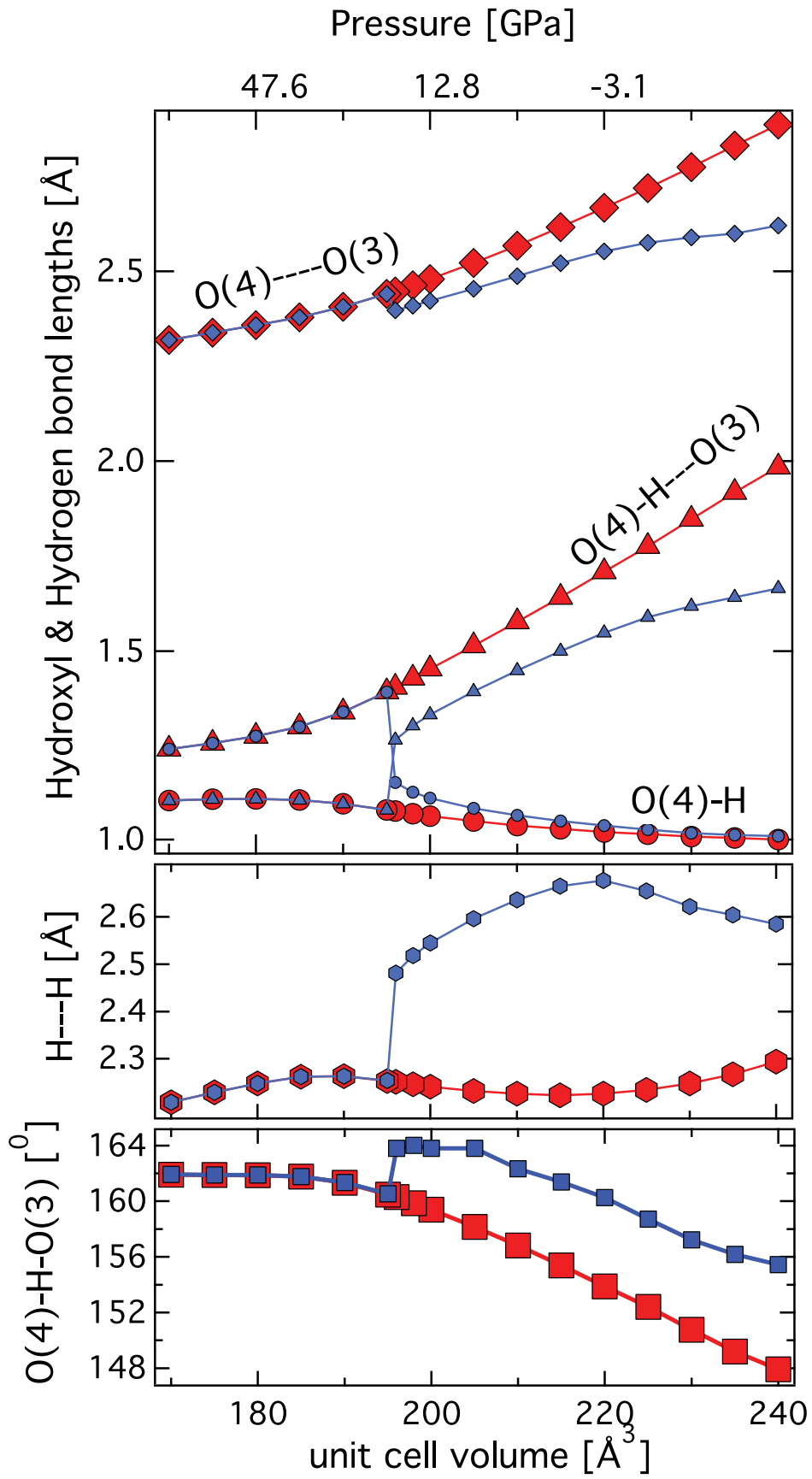

Figure 2

This is a preprint, the final version is subject to change, of the American Mineralogist (MSA)
Cite as Authors (Year) Title. American Mineralogist, in press.
DOI: https://doi.org/10.2138/am-2019-6694

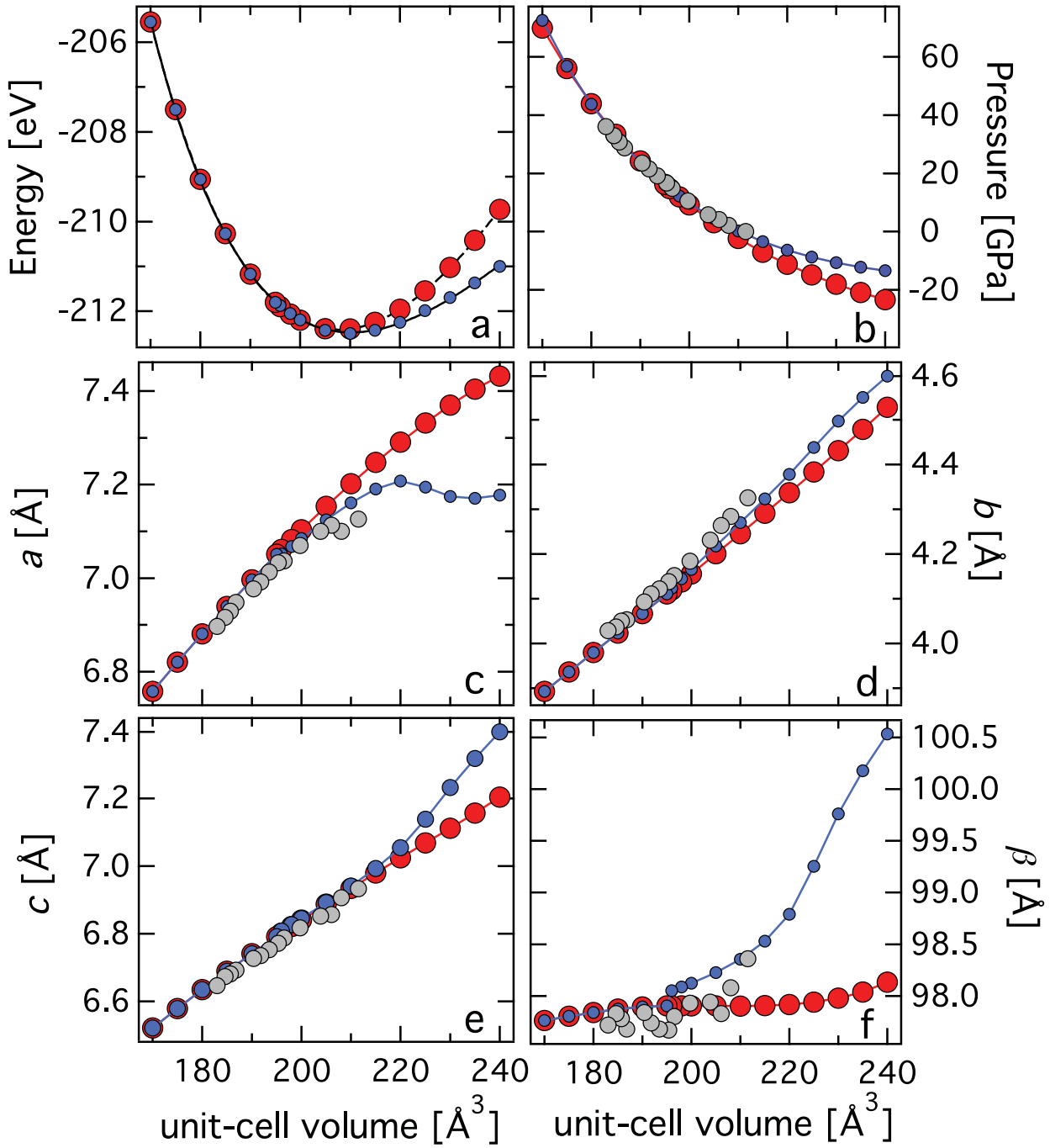

Figure 3

This is a preprint, the final version is subject to change, of the American Mineralogist (MSA)
Cite as Authors (Year) Title. American Mineralogist, in press.
DOI: https://doi.org/10.2138/am-2019-6694

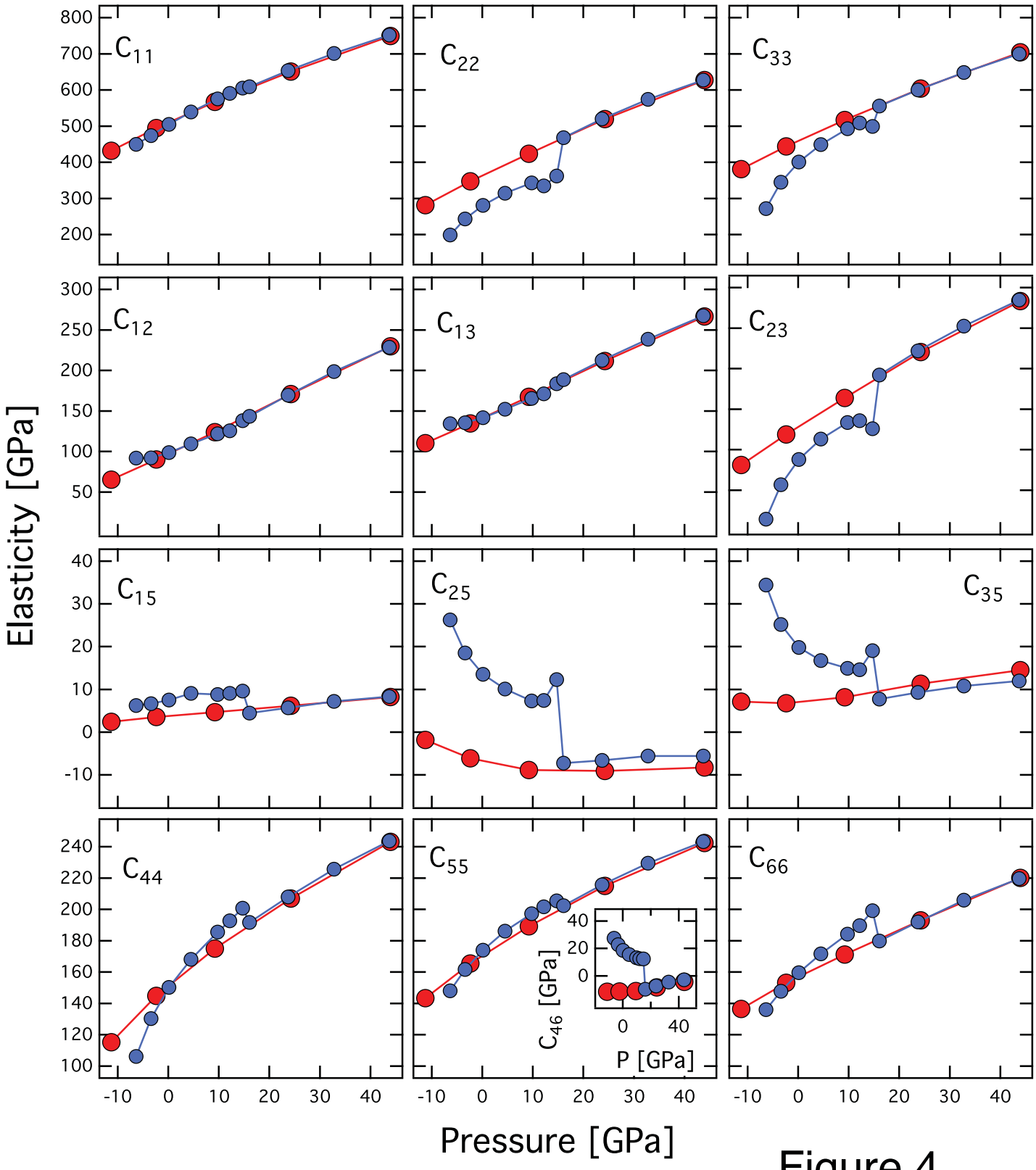

Figure 4

This is a preprint, the final version is subject to change, of the American Mineralogist (MSA)
Cite as Authors (Year) Title. American Mineralogist, in press.
DOI: https://doi.org/10.2138/am-2019-6694

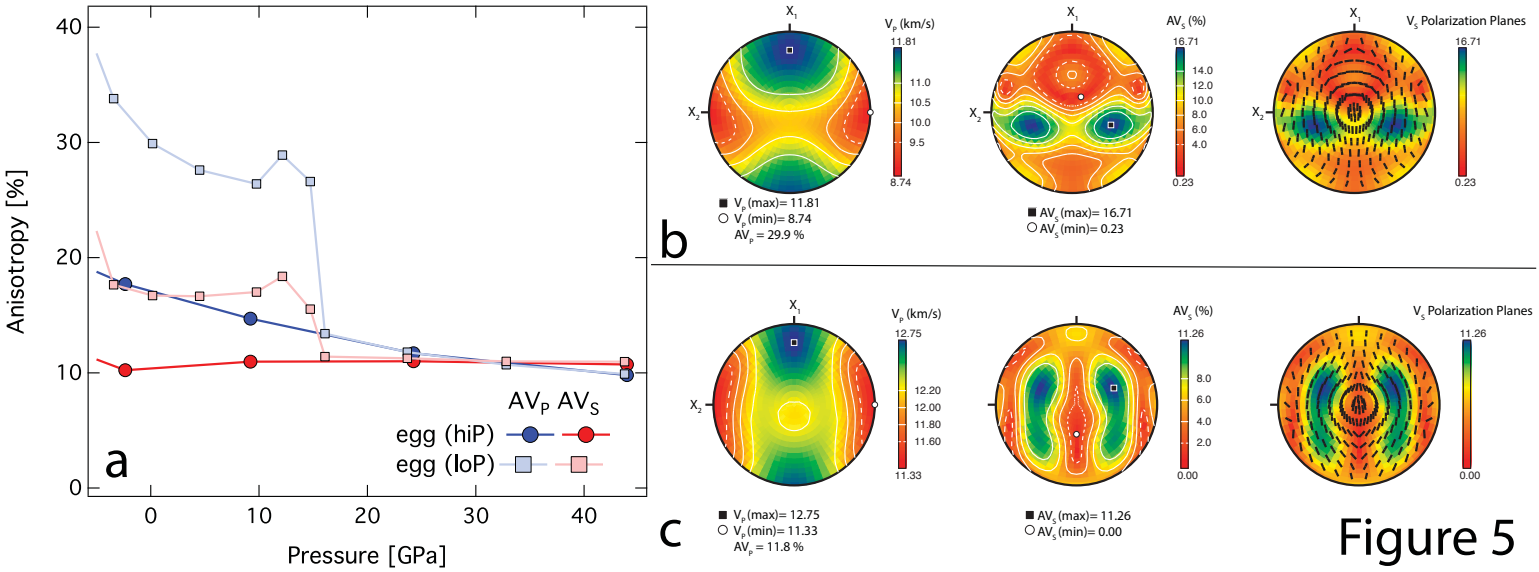

Figure 5

This is a preprint, the final version is subject to change, of the American Mineralogist (MSA)
Cite as Authors (Year) Title. American Mineralogist, in press.
DOI: https://doi.org/10.2138/am-2019-6694

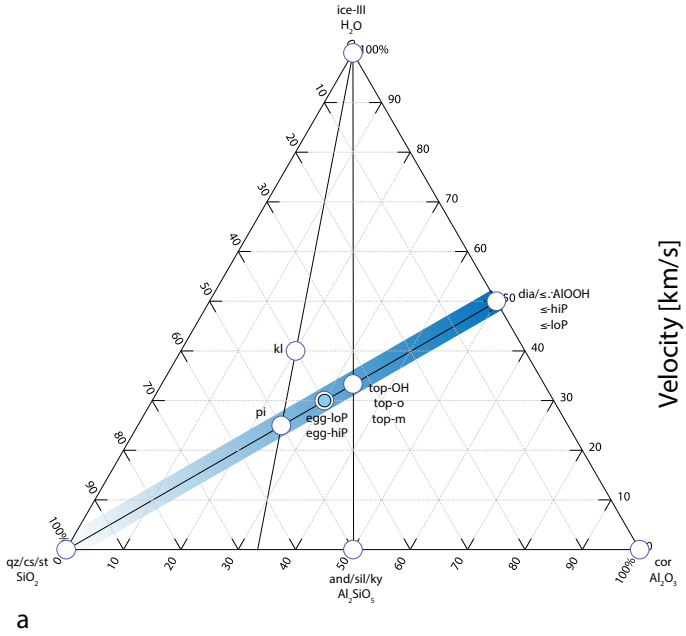

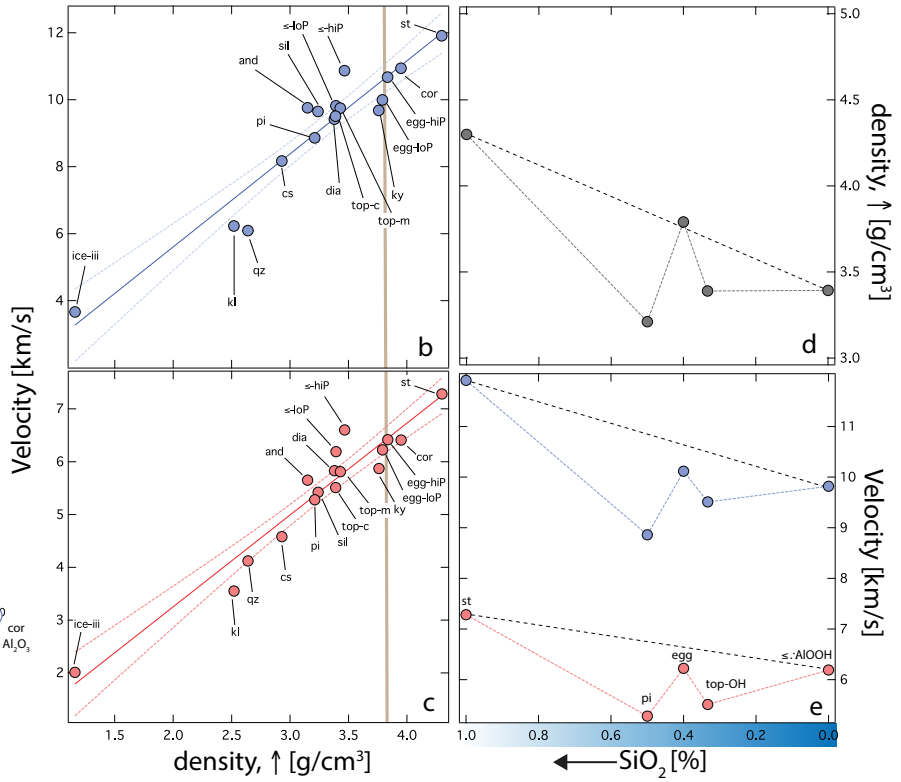

Figure 6

This is a preprint, the final version is subject to change, of the American Mineralogist (MSA)
Cite as Authors (Year) Title. American Mineralogist, in press.
DOI: https://doi.org/10.2138/am-2019-6694

Figure 7